Force-Field Development and Molecular Dynamics of [NiFe] Hydrogenase

Dayle M. A. Smith,* Yijia Xiong, T. P. Straatsma, Kevin M. Rosso, and Thomas C. Squier

Pacific Northwest National Laboratory, P.O. Box 999, MSIN J4-33, Richland, Washington 99352, United States

S Supporting Information

ABSTRACT: Classical molecular force-field parameters describing the structure and motion of metal clusters in [NiFe] hydrogenase enzymes can be used to compare the dynamics and thermodynamics of [NiFe] under different oxidation, protonation, and ligation circumstances. Using density functional theory (DFT) calculations of small model clusters representative of the active site and the proximal, medial, and distal Fe/S metal centers and their attached protein side chains, we have calculated classical force-field parameters for [NiFe] in reduced and oxidized states, including internal coordinates, force constants, and atom-centered charges. Derived force constants revealed that cysteinate ligands bound to the metal ions are more flexible in the Ni−B active site, which has a bridging hydroxide ligand, than in the Ni−C active site, which has a bridging hydride. Ten nanosecond all-atom, explicit-solvent MD simulations of [NiFe] hydrogenase in oxidized and reduced catalytic states established the stability of the derived force-field parameters in terms of $C\alpha$ and metal cluster fluctuations. Average active site structures from the protein MD simulations are consistent with [NiFe] structures from the Protein Data Bank, suggesting that the derived force-field parameters are transferrable to other hydrogenases beyond the structure used for testing. A comparison of experimental H_2-production rates demonstrated a relationship between cysteine side chain rotation and activity, justifying the use of a fully dynamic model of [NiFe] metal cluster motion.

Hydrogenase enzymes catalyze the reversible oxidation of dihydrogen into protons and electrons and therefore have potential for use in hydrogen-based energy generation.[1] High resolution crystal structures of [NiFe] hydrogenases stabilized in different geometries, charges, and spin states of the metal centers,[2−14] in conjunction with spectroscopic measurements, have been useful for elucidating the redox states and reaction mechanism of [NiFe] hydrogenase.[15] The current understanding of the structural changes within the active sites of hydrogenases that are associated with enzyme activation primarily rely on comparisons between infrared and electron paramagnetic resonance (EPR) spectroscopic measurements under defined redox conditions.[16] It is understood that the active sites of the two main types of hydrogenases ([FeFe] and [NiFe]) are able to acquire different structures, either catalytically active or inactive, within a relatively narrow range of redox potentials that involve changes in the geometry of the metal sites.[15,17,18] Physical description of hydrogenase metallocluster motion and how it relates to changes in amino acid sequence, oxidation, or protonation state can clarify the mechanism of [NiFe] hydrogenase at a molecular level and also inform the development of small biomimetic catalysts.[19−22]

Molecular simulations of [NiFe] hydrogenases using classical force fields have helped improve our understanding of gas channels through the protein, leading to the identification of key residues that control gas transport (and therefore the crucial oxygen sensitivity).[23−25] Since these computational studies were concerned with the properties of the protein (nonmetallic) residues, it was appropriate to freeze the internal coordinates[23] of the metal centers or copy force-field parameters from other molecules.[25] In contrast, our aim is to describe the dynamics of the metal centers themselves and how they couple with the protein matrix.

A fully dynamic classical mechanical (CM) atomistic description of a molecule requires knowledge of its interatomic potential energy variables such as force constants (k_r, k_θ, k_φ), equilibrium (ideal) bond lengths and angles (r_0, θ_0), dihedral phases and periodicities (φ_0, n), charges (q_i), Lennard-Jones radii (σ_{ij}), and well depths (ε_{ij}), such as those described by the AMBER[26] model of molecular motion (eq 1). Accordingly, we have used density functional theory (DFT) calculations on small model clusters representative of the metal sites in [NiFe] hydrogenase to develop these classical parameters and have tested them using classical molecular dynamics (MD) simulations of isolated model clusters and in all-atom, explicit solvent simulations of complete [NiFe] hydrogenase enzymes in the oxidized and reduced Ni−B and Ni−C catalytic states. We have also done an extensive survey of [NiFe] structures in the Protein Data Bank and a literature review of [NiFe] H_2-production rates to compare active site structures from our simulations against a larger set of structures and to see if there are internal coordinates that correlate with catalytic activity.

$$U = \sum_{\text{bonds}} k_r(r - r_0)^2 + \sum_{\text{angles}} k_\theta(\theta - \theta_0)^2 + \sum_{\text{dihedrals}} k_\varphi$$

$$\times [1 + \cos(n\varphi + \varphi_0)] + \sum_i \sum_{i \neq j} 4\varepsilon_{ij}\left[\left(\frac{\sigma_{ij}}{r_{ij}}\right)^{12} - \left(\frac{\sigma_{ij}}{r_{ij}}\right)^6\right]$$

$$+ \sum_i \sum_{i \neq j} \frac{q_i q_j}{\varepsilon_0 r_{ij}}$$

AMBER potential energy function

(1)

[NiFe] hydrogenase enzymes are heterodimers, consisting of a 34 kDa small subunit and 61 kDa large subunit (Figure 1).
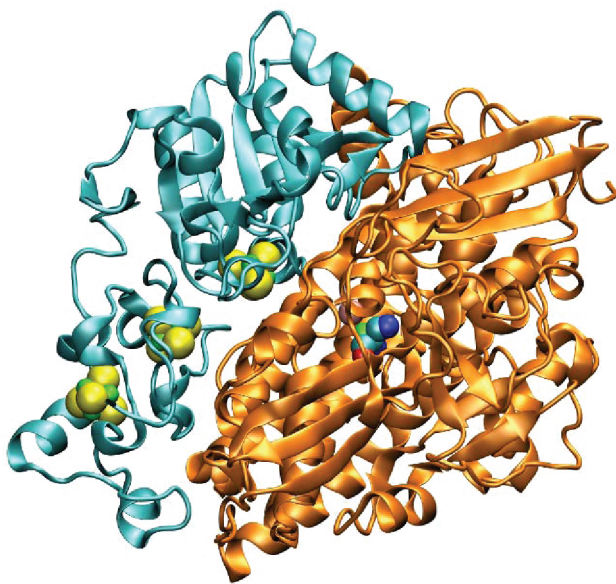

Figure 1. [NiFe] structure 1YRQ.pdb.[31] Protein residues are shown in ribbons format. Orange, large subunit; cyan, small subunit. Nonprotein atoms are shown as van der Waals spheres. Green = iron, silver = nickel, yellow = sulfur, cyan = carbon, blue = nitrogen, and red = oxygen.

The small subunit contains three iron–sulfur (Fe/S) clusters forming an electron transfer chain that shuttles electrons from cellular redox donors (e.g., membrane bound cytochromes) to the bimetallic active site in the large subunit. The active site consists of a nickel ion, an iron ion, three nonprotein diatomic ligands bound to the iron, two cysteinates (deprotonated cysteines) bridging the two metals, and two cysteinates bound only to the nickel atom (terminal cysteinates). As part of the reaction mechanism, which involves redox-dependent changes in the geometry around the active site metals, a bridging ligand can bind between the Fe and Ni metals.[23,25,27,28] According to EPR experiments,[29] the oxidized form of [NiFe] contains a mixture of catalytically inactive Ni–A ("unready") and Ni–B ("ready") forms which convert to the reduced Ni–C ("active") state after passing through an EPR-silent state (Ni–Si) and then to the fully reduced, catalytically active Ni–L state. The iron ion has +2 formal charge; the nickel ion has +3 formal charge, and $S = 1/2$ in the EPR-active Ni–A, Ni–B, and Ni–C states. The bridging ligands are hydroxide and hydride in Ni–B (oxidized) and Ni–C (reduced) active sites, respectively.[10,15,29,30] The active site can have an overall high- or low-spin d-electron

configuration depending on the arrangement of the cysteinate ligands around the nickel.[15] In this study, we assumed the low-spin active site electron configuration (as in ref 23) corresponding to a distorted square pyramidal ligand arrangement around Ni.

While possessing similar architectures, differences in the potentials of each of the three Fe/S clusters arise due to differences in bound ligands. The proximal Fe/S cluster near the active site is a canonical Fe_4S_4 cluster with each iron bound to the protein via a cysteinate $S\gamma$. In comparison, the medial Fe_3S_4 cluster lacks one iron, while the distal Fe/S cluster has one cysteinate substituted by a histidine protonated at $N\varepsilon$.[31] The iron atoms in the Fe/S clusters can have a +2 or +3 formal charge and have an antiferromagnetic electron configuration,[32,33] meaning that each iron is high-spin and they couple together antiparallel to form a net low-spin. On the basis of vibrational and electron paramagnetic resonance spectroscopy,[15] [NiFe] hydrogenases in the inactive states have oxidized Fe/S clusters, whereas the active states have reduced Fe/S clusters. The medial cluster has a high reduction potential compared to the Fe_4S_4 clusters, and changing the medial cluster from Fe_3S_4 to Fe_4S_4 switches its reduction potential from negative to positive,[7] more in line with the other Fe/S clusters. Therefore, both oxidation states of the medial cluster are included in this study to enable future comparison simulations.

METHODS

Calculations of the force-field parameters were done with small model clusters using DFT. Equilibrium (ideal) bond lengths, angles, and dihedral phases were calculated using internal coordinate generation from DFT optimized geometries. Atom-centered charges were calculated by fitting point charges to DFT electrostatic potentials. Force constants were calculated using frequency matching. Individual model cluster and full [NiFe] protein MD simulations were done for testing purposes. A survey of [NiFe] protein structures and H_2-production rates was done to compare the active site structures from the protein MD simulations against a larger set of structures to test for transferability and to look for active site internal coordinates that differ with activity.

Model Building. Model metal clusters were built by extracting the coordinates from a [NiFe] structure (Figure 1) determined by X-ray crystallography in the Protein Data Bank (PDB ID 1YRQ, 1.83 Å resolution, oxidized catalytic state).[31] Cysteinate and histidine ligands were truncated at $C\beta$ by replacing side chains with thiolates and imidazole, respectively. We have parametrized oxidized and reduced Fe/S clusters and active sites using hydroxide and hydride bridging ligands (Ni–B and Ni–C). Table 1 summarizes metal cluster oxidation states

Table 1. [NiFe] Metal Cluster Names, Ligands, Oxidation, and Spin States

| name	abbreviation	metals	ligands	charge	multiplicity
oxidized, proximal Fe/S	SPO	Fe3+, Fe3+, Fe2+, Fe2+	4 Cys-	−2	1
reduced, proximal Fe/S	SPR	Fe3+, Fe2+, Fe2+, Fe2+	4 Cys-	−3	2
oxidized, medial Fe/S	F3O	Fe3+, Fe3+, Fe3+	3 Cys-	−2	6
reduced, medial Fe/S	F3R	Fe3+, Fe3+, Fe2+	3 Cys-	−3	5
oxidized, distal Fe/S	SDO	Fe3+, Fe3+, Fe2+, Fe2+	4 Cys-, His	−1	1
reduced, distal Fe/S	SDR	Fe3+, Fe2+, Fe2+, Fe2+	4 Cys-, His	−2	2
Ni–B active site	NFB	Fe2+, Ni3+	4 Cys-, CO, 2 CN-, OH-	−2	2
Ni–C active site	NFC	Fe2+, Ni3+	4 Cys-, CO, 2 CN-, H-	−2	2
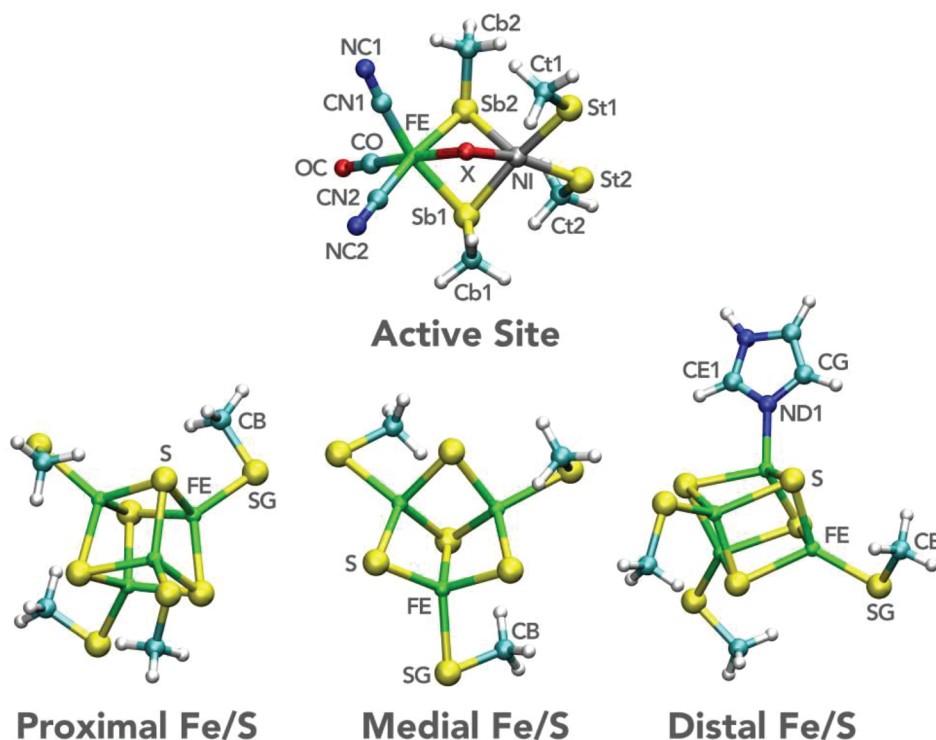
Figure 2. Models of [NiFe] metal clusters used for DFT parametrization with atom names labeled. Protein side chain atoms have atom types from the AMBER force field, and the non-protein atom types are the same as the atom names. In the active site model, X = OH- and H- for Ni–B and Ni–C, respectively, and bridging ligand atom names are "XO" for hydroxide oxygen and "XH" hydride or hydroxide hydrogen atoms. Green = iron, silver = nickel, yellow = sulfur, cyan = carbon, blue = nitrogen, and red = oxygen.

and nomenclature, and Figure 2 describes the model clusters, atom names, and atom types.

To test the parameters *in situ*, we built solvated structures of [NiFe] hydrogenase in the Ni–B and Ni–C catalytic states using the 1YRQ structure.[31] Histidine protonation states were determined using PropKa[34] and visual inspection. This analysis showed that histidines 184 of the small subunit and 79 in the large subunit are protonated at Nε; histidines 61 and 192 of the small subunit and 204, 210, and 549 of the large subunit are protonated at both Nδ and Nε; the rest are protonated at Nδ. The protein was inserted into a cubic box with minimum 12 Å distance between the protein and the side of the box, and then, the box was then filled with water molecules. The aqueous protein systems were neutralized by replacing water molecules with sodium ions at minima of the protein's electrostatic potential (one sodium ion for Ni–B and four for Ni–C). These solvated, neutralized proteins were used for the MD simulations described below.

DFT Calculations. All DFT calculations were done with the NWChem computational chemistry software[35] using the BLYP functional, as described previously in the parametrization of the [FeFe] hydrogenase.[36] All calculations used default NWChem DFT electron density convergence criteria. Initial molecular orbitals of the active site models were generated using a guess calculated from superimposed density matrices of the atoms (*atomic* initial guess) based on neutral nonmetal atoms and cationic metal atoms using the *atomscf* setting. Initial molecular orbitals for the iron–sulfur model clusters were calculated using a fragment guess built from converged molecular orbitals of Fe_3S_4, Fe_4S_4, thiolate, and imidazole molecules. Initial molecular orbitals for the fragments were calculated using an *atomic* guess, except for Fe_4S_4. Fe_3S_4 molecular orbitals

converged to an antiferromagnetic electron configuration; however, Fe_4S_4 orbitals converged to a ferromagnetic low-spin electron configuration. Therefore, we used a fragment guess to calculate Fe_4S_4 orbitals from Fe_3S_4 and Fe(III) orbitals, which converged to the desired antiferromagnetic configuration.

These force-field development tasks required a large number of DFT calculations, so we did a basis set comparison to find basis sets appropriate for calculation of equilibrium internal coordinates and force constants. Using Ni–C and reduced distal Fe/S cluster models, we performed geometry optimizations and harmonic frequency calculations with two basis sets. Geometry optimizations were done using the NWChem *driver* module with default convergence criteria for gradients and coordinate displacements, except for the geometry optimizations prior to harmonic frequency calculations, which were done using convergence thresholds defined by the *tight* keyword. The larger basis is triple-ζ with diffuse and polarization functions[37,38] and has 688 basis functions for the Ni–C model and 861 for the distal Fe/S cluster model. The smaller basis set is double-ζ[37,39] and does not include polarization functions (279 functions for the Ni–C model and 346 for the distal Fe/S cluster model). The NI–FE distance in the active site model is 2.64 Å with the larger basis set and 2.69 Å using the smaller one; the FE–SG distance in the reduced distal Fe/S model cluster was 2.32 Å using the larger basis set and 2.35 Å using the smaller one. The zero-point energy of the Ni–C active site model was 115.0 kcal/mol with the larger basis set and 115.9 kcal/mol with the smaller one; the zero-point energy of the distal cluster was 120.1 kcal/mol using the larger basis and 122.8 using the smaller one. On the basis of this comparison, we used the larger basis set to

calculate equilibrium internal coordinates, which only need to be calculated once, and used the smaller one for the force constant calculations, which required multiple harmonic frequency and geometry optimization calculations.

Internal Coordinates. DFT optimized structures were read into the VMD 1.8.6 program[40] to define atom connectivity and calculate equilibrium (ideal) internal coordinates (r_0, θ_0, and φ_0) using the *parametrization tool*. We did not connect Fe/S cluster iron atoms or sulfur atoms, so no FE—FE or S—S bonds were generated. However, we did connect NI and FE atoms in the active site models since this coordinate is characteristic of the different active site catalytic states[30] and because the NI—FE vector is a convenient point-of-reference for angles and dihedrals describing side chain ligand rotation. We chose to use all of the generated bonds and angles to describe the motion of model clusters; however, we chose a select subset of dihedral angles since each model cluster has >100 dihedrals. Specifically, we included only those dihedrals describing the rotation of the metal centers in the protein matrix. For the Fe/S clusters, we included S—FE—SG—CB and FE—S—FE—SG dihedral angles to describe thiolate rotation and S—FE—ND1—(CE1 or CG) and FE—S—FE—ND1 dihedral angles to describe imidazole rotation. For the active site models, we chose FE—NI—Sb—Cb, FE—NI—St—Ct, and Sb—FE—NI—St dihedral angles to describe thiolate rotation, in which b and t designate bridging and terminal thiolates, respectively (Figure 2). The Fe/S S—FE—SG—CB and S—FE—ND1—(CE1 or CG) dihedrals are similar to the minima of a periodic function with periodicity = 3. FE—S—FE—SG and FE—S—FE—ND1 dihedrals are ±140, on average, which fits the minima of an $n = 5$, $\varphi_0 = 180$ dihedral potential. Active site dihedral potentials have $n = 1$ with phases determined by the dihedral angles from the geometry optimization.

Atom Types. We determined unique atom types based on the internal coordinates. Upon comparison of the Fe/S cluster internal coordinates, it was apparent that each of the Fe/S clusters can be defined by a small number of unique internal coordinates, assuming that the FE—S and FE—SG bonds, S—FE—S and S—FE—SG angles, and S—FE—SG—CB and FE—S—FE—SG dihedrals (and corresponding histidine dihedrals) are similar. Unlike the Fe/S clusters, the evaluation of active site internal coordinates revealed that a larger number of unique atoms is required, as in the [FeFe] active site.[36] For instance, two of the four CN—FE—Sb angles are nearly linear, whereas the others are less than 90°, and there are two different values for Sb—NI—St angles, which infers unique types for all of the active site heavy atoms.

Atom-Centered Charges. The standard procedure for deriving atom-centered charges for the AMBER force field is to do a Hartree—Fock self-consistent field (SCF) geometry optimization with the 6-31G* basis set followed by two-stage fitting of the SCF electrostatic potential to point charges using the restrained electrostatic potential fitting method (RESP).[41] However, the geometry of the distal Fe/S cluster optimized with SCF is inconsistent with the one using the larger basis set and DFT. Specifically, the imidazole of the distal Fe/S cluster model does not remain perpendicular to the Fe₄S₄ cluster. Therefore, we chose to use BLYP with 6-31G* to calculate the charges (previously used to derive heme charges[42]) which gave improved geometries; the resulting structures have root-mean-squared deviations of less than 0.3 Å from the structures calculated from the triple-ζ basis set. Previous calculations of [NiFe] active site charges used a similar DFT functional and

similar basis sets for charge calculations (B3LYP/6-31+G(d)[23] and B3LYP/6-31G*[25]).

Electrostatic potentials were calculated using default probe and atomic radii (probe radius = 0.7 Å; atomic radii = 0.3, 0.77, 0.66, 1.04, 1.15, and 1.17 Å for H, C, O, S, Fe, and Ni atoms, respectively). The RESP fitting involves the selection of fitting constraints. For each of the Fe/S clusters, we constrained equivalent FE, SG, and CB atoms to have the same charge. For the distal cluster, no constraints were made on the imidazole atoms. For the active site models, we considered both cyanide carbons and both cyanide nitrogens to have equal charges. The two bridging thiolates were considered unique from the terminal thiolates, and the similar cysteinate sulfur and carbon atoms were constrained to have equal charge.

Since the charges were calculated using the model clusters with Cβ atoms replaced with hydrogen and do not include backbone atoms, insertion of the metal clusters into the proteins required an adjustment to make the atoms in each cluster add up to an integer. Therefore, a small residual charge was added to the Cβ atoms ("charge patching") in each cluster.

Lennard-Jones Parameters. We copied the Lennard-Jones radii and well depths for thiolate and imidazole S, C, N, O, and H atoms from the AMBER cysteine and histidine atoms. Cyanide, carbon monoxide, and bridging ligand Lenard-Jones parameters were copied from those of corresponding backbone atoms; Fe/S cluster S was copied from cysteine. Lennard-Jones parameters for the NI and FE metals were taken from ref 43.

Force Constants. We derived bond, angle, and dihedral force constants for metal clusters using the automated frequency-matching method (AFMM[43,44]). This method uses a Monte Carlo algorithm to find force-field parameters that yield classical normal modes that best match a reference set of quantum mechanical (QM) modes and frequencies. AFMM optimization works by finding the QM mode that best overlaps with each CM mode and minimizing the root-mean-square deviation, σ, between their respective frequencies. AFMM is a Python program that reads DFT normal modes and calls a CM program to calculate normal modes during each iterative step. The program is written for the CHARMM[45] CM program and can read output from NWChem DFT harmonic frequency calculations. We found the potential energy distribution (PED) analysis capability of CHARMM to be useful for periodically comparing and checking the normal modes from the derived parameters during the optimization process.

A molecular force field does not have a unique solution. Animation of the model cluster DFT normal modes showed that the low-frequency (<1000 cm^{-1}) modes include contributions from multiple bond, angle, and dihedral coordinates with unknown force constants. Therefore, we derived initial k_r and k_θ force constants prior to frequency matching by calculating relaxed potential energy (PE) curves for each of the unique bonds and angles in an effort to start the optimization from an unbiased initial guess. The distal Fe/S cluster contains all of the initial internal coordinates of the other Fe/S clusters, so we used the reduced distal cluster model to scan the unique Fe/S cluster internal coordinates. We used the Ni—C state for the bulk of the active site potential energy scans and calculated PE curves for the bonds and angles involving hydroxide atoms using the Ni—B model active site. Curve fitting for all of the PE curves was done using a least-squares method. We fit 20 data points for each bond and angle curve using a 0.02 Å bond spacing and 2° angle spacing to ensure sampling at the harmonic portion of each potential

energy well. We found the NWChem *geometry adjust* capability to be very useful for updating the geometries at each step from the optimized geometry at the previous step. The bond and angle force constants were derived from the PE scans by fitting to $U(r) = k_r(r - r_0)^2$ and $U(\theta) = k_\theta(\theta - \theta_0)^2$, respectively, by first subtracting the energies from the minimum energy and multiplying by 627.51 to convert Hartrees to kcal/mol. We used 10 kcal/mol for the initial dihedral force constants.

Using the aforementioned initial force constants, atom-centered charges, Lennard-Jones parameters, and DFT equilibrium internal coordinates (r_0, θ_0, and φ_0 from the structures used in the harmonic frequency calculations), we built CHARMM topologies and parameter files for the model clusters for use with the AFMM Python script. We included electrostatic interactions between atoms more than three bonds apart (1−4 interactions) using a cutoff distance of 12 Å. Rather than match the frequencies of all eight metal clusters, we limited this effort to include only the Ni−B and Ni−C active sites and the reduced Fe/S clusters.

AFMM optimization requires specification of a range of parameter values as well as an initial value. In the first 2000-step optimization stage, bond and angle force constants were allowed to range ±50%. Dihedral force constants were allowed to range from 1 to 25 kcal/mol for all except the more rigid FE−NI−Sb−Cb dihedrals, which were allowed to range between 1 and 100 kcal/mol. After this first AFMM optimization stage, we compared the similar force constants to each other and to the PE scan force constants, adjusted some force constants as appropriate, then ran another set of 2000-step optimizations, allowing all of the force constants to vary by ±50%. In the final three 2000-step optimizations, the force constants were varied by ±25%.

Testing. The derived parameters were tested with molecular dynamics simulations for the isolated model clusters and in full solvated protein simulations. The GROMACS 4.0[46] software (double-precision version) was selected for this task for its computational speed and trajectory analysis tools. We used the final derived force-field parameters to create GROMACS topologies for the metal clusters listed in Table 1. We ran 10 ns of NpT dynamics using a 2 fs time step and the LINCS constraint method[47] for bonds to hydrogen atoms. A constant 300 K temperature and 1 atm pressure were maintained using a Nosé−Hoover thermostat[48] and a Parrinello−Rahman barostat.[49] Electrostatic interactions were calculated using the Particle Mesh Ewald method with a cutoff of 12 Å. Lennard-Jones interactions were truncated at 12 Å. Electrostatic interactions were calculated between atoms more than three bonds apart (1−4 interactions). Coordinates were saved every picosecond, yielding a total of 10 000 frames. The trajectory was then analyzed to measure internal coordinates and average structures.

Using the AMBER03[26] force field and TIP3P solvent model[50] with the derived parameters, Ni−B and Ni−C solvated and neutralized proteins (with all-oxidized and all-reduced Fe/S clusters, respectively) were energy-minimized to a tolerance of 500 kJ/mol·nm (GROMACS units), and that structure was used as a starting point for equilibration. MD integration parameters were the same as described above for the model clusters. Equilibration was done in 250-ps steps, in which the coordinates and velocities of each equilibration step were used to initialize each subsequent step. In the first equilibration step, non-hydrogen atoms were restrained using harmonic position restraints with a force constant of 1000 kJ/mol·nm^2, and the temperature was set at 100 K. Next, the temperature was increased in 50 K increments to 300 K; then, restraint forces were reduced to zero in 200 kJ/mol·nm^2 increments. Following equilibration, the protein systems were subjected to 10 ns of molecular dynamics.

Since the active site model cluster and full-protein coordinates were extracted from a single protein structure, we also did a survey of active site angles and dihedrals from 27 additional [NiFe] hydrogenases in the Protein Data Bank and compared them to the active site structures from the DFT, model, and protein MD simulations.[2−14] We focused this analysis on the cysteinate side chains that bind to the metal atoms. In addition, we did a survey of [NiFe] activities for eight different organisms for which PDB structures are available[51−57] and looked for active site internal coordinates that correlate with catalytic activity (H_2 production).

RESULTS

Relationship between Active Site Geometry and Activity. Cysteinate arrangement around the metal ions varies among the [NiFe] structures, which themselves differ in amino acid sequence and bacterium species[2−14] (Figure 3). The
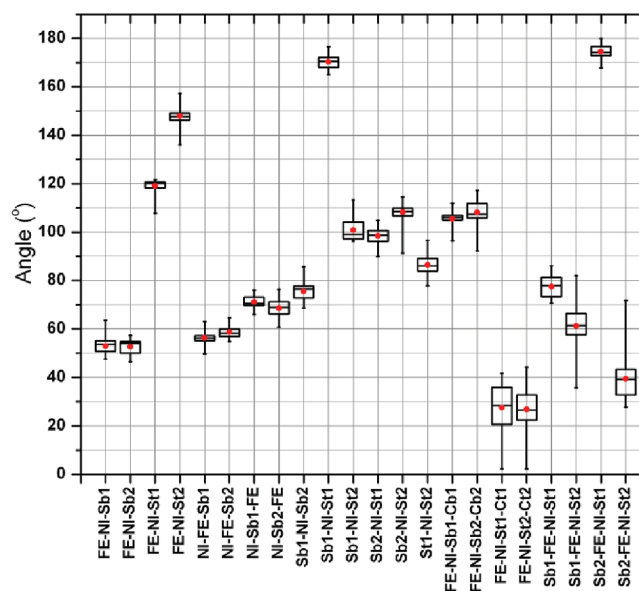

Figure 3. Metal-cysteinate active site angles from 27 [NiFe] structures in the Protein Data Bank[2−14] shown as a box plot. The boxes show lower quartile, median, and upper quartile angles. The minimum and maximum angles are vertical lines. Mean angles are red circles. See Figure 2 for atom names.

internal coordinates involving the metal ions and terminal cysteinates show a larger range of values than the bridging cysteinates because the side chains are bound to only one metal ion and are therefore sensitive to the arrangement of nearby protein atoms. Terminal cysteinates have physical significance because they are flexible enough to change the nickel d-electron configuration and gate access to its vacant binding site (see Figure 1 in ref 15).

Published [NiFe] catalytic H_2 production rates (specific activities) range between 72 and 400 μmol H_2/mg/min. Comparison of the internal coordinates in Figure 3 against these activities indicated that activity approximately varies with the orientation of the terminal cysteinate on the same side as

the bridging ligand (St1 in Figure 2; see Table 2). Hydrogenases with faster H_2 production rates have a larger

Table 2. [NiFe] Hydrogen Production Activities and Terminal Cysteinate Dihedral Angles (See Figure 2 for Atom Names)[a]

PDB ID	bacterium species	activity	Sb2-FE-NI-St1 (deg)	FE-NI-St1-Ct1(deg)
3MYR[4]	*Allochromatium vinosum*	72[51]	74	42
3AYX[56]	*Hydrogenovibrio marinus*	185[56]	84	20
1FRF[56]	*Desulfovibrio fructosovorans*	205[56]	72	34
3H3X[52]	*Desulfovibrio fructosovorans*	233[52]	74	32
3CUR[6]	*Desulfovibrio fructosovorans*	260[6]	71	28
1H2R[53]	*Desulfovibrio vulgaris Miyazaki F*	330[54]	83	18
1YRQ[42]	*Desulfovibrio fructosovorans*	330[56]	76	34
3CUS[6]	*Desulfovibrio fructosovorans*	352[6]	79	21
1FRV[57]	*Desulfovibrio gigas*	400[55]	85	2

[a]Specific activities have units of μmol H_2/mg/min.

Sb2−FE−NI−St1 dihedral and a smaller FE−NI−St1−Ct1 dihedral.

If the derived active site parameters are flexible enough to allow the active site ligand arrangement to adjust in a realistic way to the presence of atoms beyond those used to derive the parameters, the force field should be transferrable to other hydrogenases with different amino acid sequences and will allow for predictions of mutated protein structures. Our calculations show that the range of active site metal-cysteinate angles explored during dynamics depends on oxidation state (Ni−B vs Ni−C).

Comparison of DFT Results with Previous Calculations. The final model cluster internal coordinates and spin densities are similar to previously published values.[30,58,59] The NI−FE distances for the Ni−B and Ni−C active site models are 2.99 and 2.64 Å, respectively, and the DFT study in ref 30 reported optimized distances of 3.05 and 2.67 Å. FE−S and FE−SG bonds are 2.33 ± 0.4 Å, and FE−ND1 distances are 0.3 Å shorter than FE−SG, comparable to ref 60.

The Fe/S cluster orbitals converged to the antiferromagnetic electron configuration with average iron spin densities of ±3.2, similar to the range described in ref 58. The unpaired spin in each of the active site models is located on the nickel atom. The nickel spin densities for the active site models are 0.59 and 0.56 electrons for Ni−B and Ni−C, respectively. Reference 30 reports slightly lower densities, 0.52 and 0.50, due to different structural and computational models.

Atom-Centered Charges. The derived charges reflect charge sharing between metal and ligand atoms relative to their formal charges.[61] Ni−B and Ni−C have Fe(II) and Ni(III), and therefore the NI charge is greater than FE in those states. NI charges are 0.76 and 0.75 electrons, and FE charges are 0.66 and 0.57 for Ni−B and Ni−C, respectively. The charges on the bridging thiolate sulfur atoms are −0.41 and −0.47 for Ni−B and Ni−C; however, the terminal thiolate sulfur atoms have more negative charge than the terminal cysteinates, −0.62 for both Ni−B and Ni−C.

The Fe/S cluster iron atoms have +2 or +3 formal charge, and the Fe/S cluster sulfur atoms have a −2 formal charge. The ranges of the FE, S, and SG charges are 0.57 to 1.05, −0.89 to −0.54, and −0.81 to −0.54 electrons, respectively. Upon reduction, the proximal and distal cluster S and SG atoms decrease by 0.14 electrons on average, but the FE atom charge increases by a smaller amount (0.08 electrons), consistent with the small change in iron electron densities described in ref 62. The charge patching required to adjust for residue backbone atoms changed the $C\beta$ charges by <0.2 electrons.

Force Constants. The PE scan potentials fit well to harmonic potentials with correlation coefficients $R^2 > 0.95$, except for the stiff diatomic stretching force constants, which have $R^2 = 0.87$. The AFMM force constant refinement optimized the force constants in the context of the electrostatic parameters, and the limited set of dihedral angles. The optimization changed the force constants by 38% for the active site models and 27% for the Fe/S cluster models, on average.

The root-mean-square deviations between CM and DFT frequencies (σ, Table 3 and Figure 4) for each of the model

Table 3. Comparison of Model Cluster Structures and Harmonic Frequencies from DFT and CM Using Derived Parameters[a]

metal cluster	RMSD (Å)	σ (cm^{-1})
oxidized, proximal Fe/S	0.20	
reduced, proximal Fe/S	0.30	35
reduced, medial Fe/S	0.27	
reduced, distal Fe/S	0.15	30
oxidized, distal Fe/S	0.11	
reduced, distal Fe/S	0.21	42
Ni−B active site	0.10	48
Ni−C active site	0.22	60

[a]RMSD: root-mean-squared deviation after superimposing non-hydrogen atoms. σ: root-mean-squared deviation of harmonic frequencies.

clusters are less than the 100 cm^{-1} threshold considered adequate based on benchmark studies.[44] It is especially important that the low-frequency torsion modes match, since only a subset of all possible dihedral angles were included in the force field.

The FE−SG force constants are larger than FE−S, which is consistent with reorganization energy calculations.[60] The FE−SG force constant is smaller in the distal cluster, which has one cysteinate replaced by a histidine (90 vs 75 kcal/mol·Å^2), and its FE−ND1 force constant is 33 kcal/mol·Å^2 larger than its FE−SG force constant. The bending force constants involving only S, SG, and FE atoms are similar between the proximal and distal clusters. However, the S−FE−SG−CB dihedral force constant is smaller in the distal cluster compared to the proximal cluster (2.1 vs 2.7 kcal/mol), and the corresponding histidine dihedral is smaller still (1.4 kcal/mol), consistent with larger amplitude histidine side chain rotation. All of the force constants for the medial cluster that involve SG and FE atoms are smaller than the corresponding values in the proximal and distal clusters, indicating that removal of one iron atom weakens the Fe/S bonded interactions with cysteinate side chains.

The different bridging ligands in Ni−B and Ni−C lead to differences between their respective force constants. The hydroxide ligand bonds to the metals have larger force

F

dx.doi.org/10.1021/ct300185u | *J. Chem. Theory Comput.* XXXX, XXX, XXX−XXX
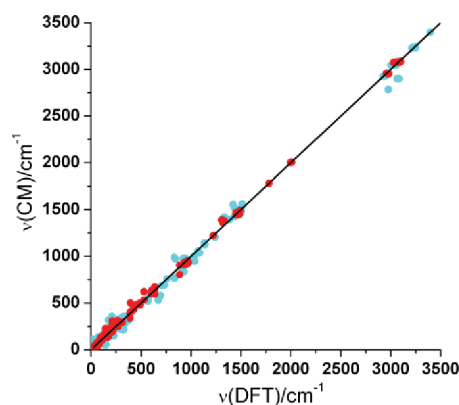
Figure 4. Frequency matching plots for Fe/S (cyan) and active site models (red). The black line represents the ideal match.

constants than the hydride ligand (FE−XO and FE−XH are 65 and 27 kcal/mol·Å^2; NI−XO and NI−XH are 71 and 34 kcal/mol·Å^2, respectively). There are 10 angles describing the motion of the bridging ligand attached to the metals, and in eight of those, the bending force constants are stiffer for the bridging hydroxide ligand than the bridging hydride ligand. Animation of the DFT normal modes and inspection of the CHARMM potential energy distributions showed that the modes with the greatest amount of XO−FE−NI and XH−FE−NI bending motion have contributions from (XO or H)−FE and (XO or H)−NI bonds. These modes have DFT frequencies of 415 and 463 cm^{-1} for XO−NI−FE and XO−FE−NI in Ni−B and 1222 and 1492 cm^{-1} for XH−NI−FE and XH−FE−NI in Ni−C and match well with the CM modes using the derived parameters (Figure 4).

The force constant optimization yielded different metal−cysteinate bending force constants for the Ni−B and Ni−C active site models. In 19 of the 21 angles and dihedrals involving metal and cysteinate sulfur atoms, the force constants are 37% smaller on average for the Ni−B model compared to the Ni−C model. For example: the FE−NI−Sb−Cb force constant is 21.9 for Ni−B and 25.3 kcal/mol for Ni−C, the FE−NI−St−Ct force constant is 2.1 for Ni−B and 4.1 kcal/mol for Ni−C, and the St1−NI−St2 force constant is 15 kcal/mol·rad^2 for Ni−B and 39 kcal/mol·rad^2 for Ni−C.

The NI−FE bond lengths for the Ni−B and Ni−C active site models are different (2.99 vs 2.64 Å); however, the force constants are very low and are nearly identical (19 and 20 kcal/mol·Å^2 for Ni−B and Ni−C, respectively). We tested whether or not the internal coordinates including the NI−FE bond are necessary by optimizing the active site models without them. We found that the NI−FE bonds and angles can be removed without affecting the optimized structure. However, without the NI−FE dihedrals, the thiolates rotated unreasonably far from their equilibrium angles. Using Sb−NI−Sb−Cb and Sb−NI−St−Ct dihedrals with the same force constant as the ones derived for FE−NI−Sb−Cb and FE−NI−St−Ct (with the appropriate dihedral phases) resulted in active site structures < 0.05 Å RMSD compared to the force field with NI−FE internal coordinates included. We should point out that the force field without NI−FE coordinates was not tested *in situ* and also that the NI−FE bond may be important when applying these parameters to active sites without a bridging ligand, such as Ni−L.

Optimization of the force constants required simultaneously optimizing the force constants for the protein-only internal

coordinates, such as SG−CB, HB−CB−SG, and the histidine internal coordinates. The optimized force constants are similar to the AMBER force constants in most cases. For instance, the CB−HB force constant is 340 kcal/mol·Å^2 from AMBER and is 362 ± 9 after optimization, and the HB−CB−HB force constant is 35 kcal/mol·rad^2 in AMBER and 37 ± 0.4 after optimization. The one force constant that changed significantly was the SG−CB force constant, which is 237 in AMBER and 161 ± 3.9 kcal/mol·Å^2 after matching the force constants to the DFT frequencies. In addition, the average SG−CB bond length is 1.87 Å in the DFT-optimized structures and is 1.81 Å in AMBER, indicating that cysteine Sγ deprotonation loosens the SG−CB bond.

Testing: Energy-Minimized Model Cluster Structures. Energy-minimized model cluster structures calculated from the derived parameters overlap well with the DFT-optimized structures (Table 3), as evidenced by the root-mean-squared deviations between non-hydrogen atoms, which are less than 0.3 Å. For the Fe/S clusters, the RMSD is mostly due to deviations of the DFT geometry optimized dihedral angles from idealized $n = 3$ periodic minima.

Testing: Neglected Dihedrals. Fe/S cluster FE−S−FE−S dihedral potentials were neglected in this study, and the model Fe/S cluster MD simulations showed that those terms were not necessary. In the model MD simulations, the average FE−S−FE−S dihedral angles are within 2° of the DFT geometry optimized values and the standard deviations are less than 4°.

According to the DFT harmonic frequency calculations, Ni−B and Ni−C have bridging ligand torsion modes (in Figure 2, this is motion up and down in the plane of the page) with small contributions from diatomic bending motion. Even though bridging ligand dihedrals were not included in our force field, the AFMM optimization produced normal modes for the torsional motion of the bridging ligands. For Ni−B, these modes are at 248 and 638 cm^{-1}, and their matching modes calculated from the derived parameters are at 286 and 627 cm^{-1}. Ni−C has bridging hydride torsion modes at 389 and 409 cm^{-1} that match with 354 and 359 cm^{-1} modes calculated from the derived parameters (Figure 4).

Dihedrals including active site diatomic ligands were not included in our derived force field. Ni−B and Ni−C protein MD did not exhibit instabilities due to nearly linear angles involving the diatomic ligands, such as NC−CN−FE or CN−FE−Sb. If researchers who use these derived parameters observe active site atoms with extremely large velocities during molecular dynamics, they should adjust the diatomic force constants[36] or add appropriate dihedral terms.

During the equilibration of the Ni−B solvated protein dynamics, the hydroxide hydrogen in Ni−B moved to the other side of the active site (Figure 2, into the page). To test whether the inversion is physically realistic, we did a 360° relaxed potential energy scan of the XH−XO−NI−FE dihedral starting from the optimized dihedral angle of 157° in 10° increments using the basis set used for the potential energy scans. According to this calculation, the inversion barrier is large (>25 kcal/mol), and the hydroxide hydrogen is sterically unlikely to move to the other side of the active site (Figure S1). We therefore considered this motion to be an artifact and restarted the equilibration using NI−FE−XO−XH and FE−NI−XO−XH dihedrals (one could also use frozen bridging ligand internal coordinates during the equilibration phase). The hydroxide dihedrals were removed after equilibration, and the

active site hydroxide did not invert during production dynamics.

Testing: Comparison with Initial Protein Structure 1YRQ.pdb and Other [NiFe] Hydrogenases. The root-mean-squared deviations (RMSD) of [NiFe] hydrogenase $C\alpha$ atoms (Figure 5) relative to the initial 1YRQ structure over the
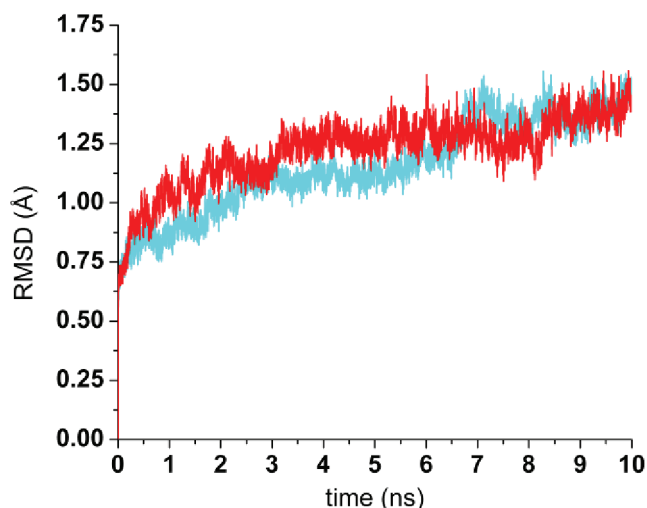

Figure 5. RMSD of [NiFe] $C\alpha$ atoms after superimposing $C\alpha$ atoms relative to 1YRQ.pdb. Cyan: Ni–B, Red: Ni–C.

10 ns simulations approach 1.5 Å (as in ref 25) after 5 ns. Trajectory animation revealed that the ∼0.25 Å fluctuations in the RMSD are due to the motion of solvent-exposed unstructured regions. The average distances between the metal clusters are tabulated in Table 4. In each state, the

Table 4. Average Distances between Centers of Mass of Metal Clusters (Å) from the Ni–B and Ni–C Protein MD Simulations and the Initial 1YRQ.pdb Structure Calculated from 5 to 10 ns

	NiB	NiC	1YRQ.pdb
active site- proximal Fe/S	15.1 + 0.2	14.8 + 0.2	14.4
proximal Fe/S- medial Fe/S	12.2 + 0.2	12.9 + 0.3	12.4
medial Fe/S- distal Fe/S	11.7 + 0.2	11.2 + 0.3	11.1

backbone RMSD and intercluster distances show little derivation from the initial structure.

Figure 6 shows snapshots of the metal clusters from the Ni–B protein MD simulations superimposed onto the initial structure from the 1YRQ.pdb Ni–B [NiFe] hydrogenase. The time-averaged active site structure has a RMSD of 0.2 Å relative to the initial structure, and this subtle discrepancy is due to the shorter NI–FE bond in 1YRQ (2.88 Å) compared to the DFT-optimized distance used in the simulation (2.99 Å).

The Fe/S cluster motion is mostly due to side chain ligand bending and rotation. The derived Fe/S cluster S–FE–SG–CB and S–FE–ND1–(CG or CE1) force constants are too large to allow for full rotation, and the dihedrals in the protein simulations maintain the minima as in the initial 1YRQ.pdb structure. On average, the S–FE–SG–CB and S–FE–ND1–(CG or CE1) dihedrals fluctuate $\pm6°$ and $\pm10°$ in the protein MD simulations. The medial cluster bending force constants are smaller than for the proximal and distal clusters so larger side chain fluctuations are apparent in the trajectory.

The active site diatomic ligands form hydrogen bonds with polar side chains nearby and the hydrogen bond distances in the protein simulations (Figure 7 and Table 5) can be used to evaluate the nonbonded parameters. One cyanide interacts with SER499 OG, the other cyanide interacts with ARG476 NH1, and the carbonyl interacts with HIS79 NE2. The SER499 and HIS79 hydrogen bond distances are similar to those in 1YRQ, although the hydrogen bonds to the charged ARG476 side chain are more than one standard deviation shorter than in 1YRQ.

In the active site models, cysteinates are replaced with thiolates, so there are no polar backbone atoms interacting with the active site. The backbone amide hydrogen atoms have a charge of 0.27 electrons in the AMBER force field, which results in electrostatic attraction between bridging cysteinate backbone NH and the sulfur on the nearest terminal cysteinate (Figure 7). The active site bridging cysteinates are resistant to rotation and maintain dihedral angles near $\pm110°$ in the protein MD simulations, similar to the survey of [NiFe] structures ($107 \pm 4°$, Figure 3). The time-averaged FE–NI–St–Ct dihedrals fluctuate $\pm20°$ in the model cluster simulations and $\pm5-6°$ in the protein simulations. Due to the NH–St hydrogen bonds, protein insertion causes metal–cysteinate angles to assume the values from the initial 1YRQ structure and the PDB survey (Table 6). In all of the angles in Table 6, Ni–B values fluctuate more than Ni–C because of the smaller Ni–B force constants.

To further compare the active site structures from these [NiFe] protein simulations against other hydrogenase structures, we have superimposed the heavy atoms of the average Ni–B and Ni–C active sites upon 1WUJ.pdb and 1WUL.pdb,[2] which are in the Ni–B and Ni–C catalytic states, respectively (Figure 8). The average Ni–B active site structure has a RMSD of 0.3 Å relative to 1WUJ, and this difference is due to the shorter NI–FE bond (2.69 Å) and the rotated terminal cysteinate ligand St1–Ct1 in 1WUJ. Also, one of the NC–CN–FE angles in the average Ni–B active site structure maintains the slightly nonlinear 176° angle from the DFT derived equilibrium angle geometry optimization, which is different from the linear angle in 1WUJ. The average Ni–C active fits 1WUL with a RMSD of 0.2 Å; both have similar NI–FE bond lengths (2.66 versus 2.57 Å for 1WUL), similar cysteinate ligand orientations and cyanide angles.

■ DISCUSSION

Comparison with [FeFe] Hydrogenase. Although the [FeFe] and [NiFe] active sites are different, both proteins have the same Fe_4S_4 clusters, and the active sites contain some similar internal coordinates that enable the comparison of the derived [NiFe] force-field parameters against [FeFe].[36] The atom-centered charges of [FeFe] were calculated using natural population analysis (NPA) of the DFT Kohn–Sham orbitals, whereas we used RESP fitting to the DFT/6-31G* electrostatic potential, and different charge derivation methods can give different results.[61] The cysteinate sulfur charges are similar (−0.81 vs −0.78 electrons for the reduced proximal cluster and −0.68 vs −0.61 for the reduced distal cluster); the reduced proximal and distal clusters have iron charges of 1.16 and 0.81 electrons, whereas the charges are 0.71 and 0.65 in [FeFe] versus [NiFe]. [FeFe] force constants were derived from diagonalization of the DFT Hessian in internal coordinates, whereas ours were derived from potential energy scans and frequency matching. The Fe/S cluster FE–SG force constant is stiffer compared to FE–S in both cases, which has been
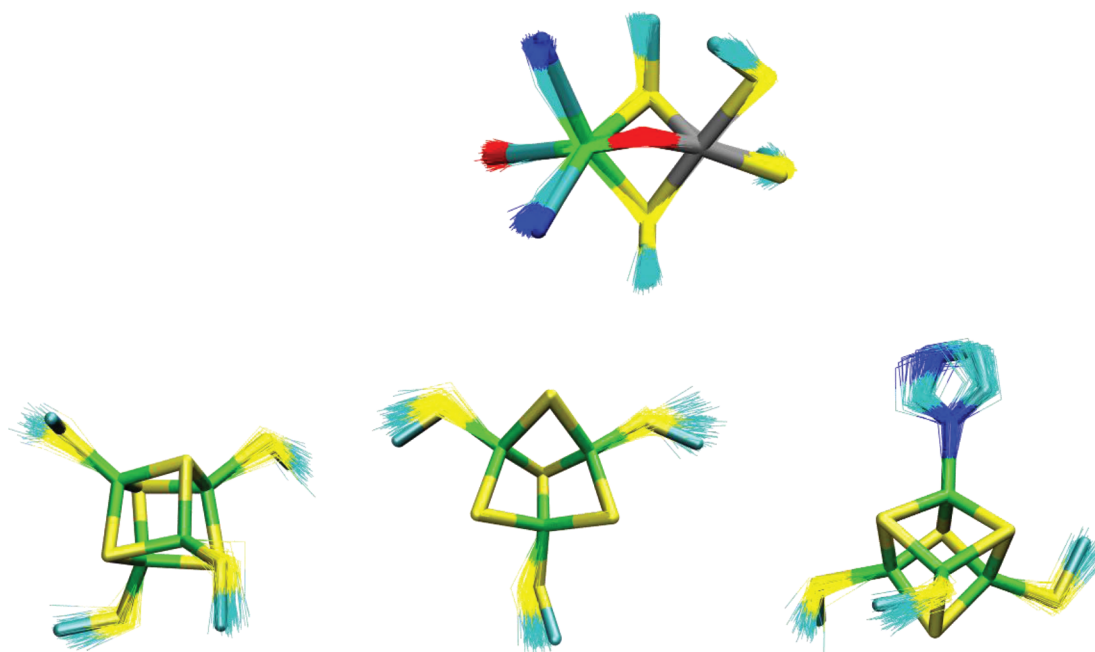
Figure 6. A total of 100 snapshots of from protein Ni−B [NiFe] MD simulation superimposed onto the initial 1YRQ structure. The initial metal cluster structures are shown as sticks, and trajectory snapshots are lines. All active site heavy atoms were superimposed. FE and S atoms were used to superimpose Fe/S clusters. Green = iron, silver = nickel, yellow = sulfur, cyan = carbon, blue = nitrogen, and red = oxygen.
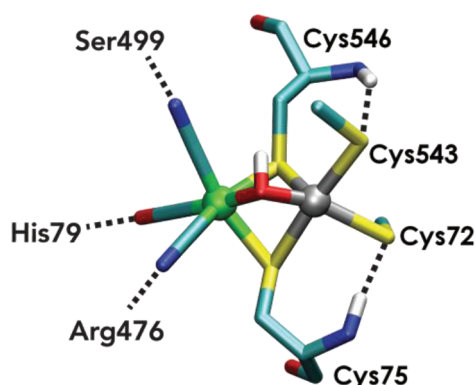

Figure 7. Hydrogen bonds to the [NiFe] active site.

Table 5. Hydrogen Bond Donor−Acceptor Distances (Å) from Protein MD Simulations and the Initial 1YRQ.pdb Structure

	Ni−B	Ni−C	1YRQ.pdb
NC1- SER499(OG)	2.74 ± 0.10	2.96 ± 0.39	2.75
NC2- ARG476(NH1)	3.12 ± 0.18	3.06 ± 0.15	3.39
OC- HIS79(NE2)	3.40 ± 0.25	3.64 ± 0.24	3.50
CYS72(SG)- CYS75(N)	3.69 ± 0.26	3.42 ± 0.15	3.33
CYS543(SG)- CYS546(N)	3.36 ± 0.16	3.83 ± 0.17	3.72

previously established in DFT reorganization energy calculations.[60] Fe/S cluster bending force constants are smaller for [FeFe] than [NiFe], due to the different methods used to derive the force constants and differences in how the connectivities were defined. [FeFe] FE−FE bonds and FE−FE−FE angles were included as well the S−FE−S−FE dihedrals that were neglected for [NiFe]. [FeFe] force constants for diatomic ligand stretching are larger than ours by a factor of 2. The optimized [NiFe] carbonyl stretching force constants (817 kcal/mol·Å² for Ni−B and 822 for Ni−C)

are between the AMBER force constant for the backbone carbonyl stretching (553 kcal/mol·Å²) and the PE scan force constant (965 kcal/mol·Å²), which seems reasonable. Force-field developers and users should be cognizant of the factor 1/2 that differs between bond and angle force constants from different derivation methods and molecular dynamics programs.

Suggested Force-Field Refinements. The hydrogen bond between NC2 and ARG476 in our Ni−B protein simulation is more than one standard deviation shorter than in the initial 1YRQ structure due to the fact that the ARG NH1 is charged. Hence, a more rigorous charge derivation that accounts for the electrostatic protein environment would improve the charges beyond the approximation that the two cyanides are equivalent. Furthermore, [NiFe] hydrogenase simulations would benefit from a quantum mechanical derivation of Lennard-Jones parameters for [NiFe]-specific atom types.

We have excluded interactions between atoms more than three bonds apart (1−4 interactions, as is customary), and we should point out that the force constants and the parsing of bonded and nonbonded contributions (eq 1) is dependent on the number of excluded electrostatic interactions. Frequency matching force constant calculations using fewer exclusions will improve the separation of bonded and nonbonded potential energy terms, although the full-protein simulations would be much more time intensive. It is also worth noting that the parsing of bonded and nonbonded parameters would benefit from additional refinement using dispersion-corrected DFT functionals.

There are active site models in addition to the two included here. The [NiFe] active site force constants should be transferrable to Ni−A and Ni−L, at least as an initial guess. The Ni−B force constants reflect the influence of a bridging oxygenic ligand on the flexibility of the attached cysteinate ligands, so the Ni−B force constants should be appropriate for Ni−A. The fully reduced Ni−L force constants can be copied from the reduced Ni−C. The force constants should provide a

Table 6. Angles between Active Site Bridging and Terminal Cysteinates (deg) from DFT; Time-Averaged Angles Protein MD Simulations; Initial Angles from 1YRQ.pdb; Average, Minimum, and Maximum Angles from the PDB Survey[2−14]

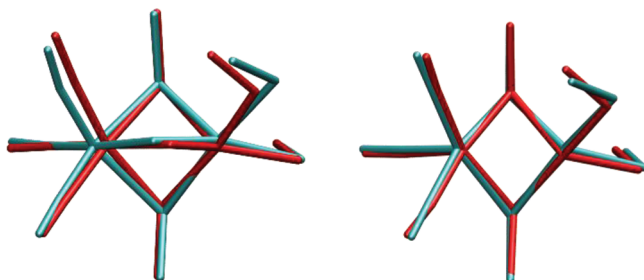|	DFT		protein MD		PDB survey			
angle	NiB	NiC	NiB	NiC	1YRQ	min	max	average
CYS75(SG)-NI-CYS72(SG)	96	99	101 ± 5	97 ± 3	100	96	113	101 ± 5
CYS546(SG)-NI-CYS543(SG)	111	117	105 ± 5	105 ± 4	100	90	105	98 ± 4
FE-NI-CYS543(SG)-CYS543(CB)	18	20	26 ± 6	20 ± 5	26	2	42	28 ± 10
FE-NI-CYS72(SG)-CYS72(CB)	13	38	32 ± 6	35 ± 5	41	2	44	28 ± 9
CYS543(SG)-FE-NI- CYS546(SG)	70	68	82 ± 5	95 ± 4	76	36	82	61 ± 8

Figure 8. Time-averaged active site structures from Ni−B (left) and Ni−C (right) [NiFe] protein MD simulations (cyan) superimposed on Ni−B and Ni−C structures 1WUJ and 1WUL (red). The bridging hydride is omitted because it was not observed in 1WUL.

good estimate for similar internal coordinates in other metalloclusters; however, it will be important to define appropriate equilibrium coordinates and charges.

It would also be helpful to extend this study to include optimized force constants for the Fe/S clusters in their oxidized states. In lieu of force constant optimization to DFT normal modes for the oxidized Fe/S clusters, one can scale up the reduced force constants by 5% to get the oxidized state's force constants according to an interpretation of ferrodoxin $[Fe_4S_4]$-Cys_4 Urey−Bradley force constants fit to vibrational spectra.[63]

■ CONCLUSIONS

Justification for a Dynamic Model of [NiFe] Metal Cluster Motion. Metal-side chain angles and dihedrals of active site terminal cysteinates show more variability than the bridging cysteinate internal coordinates from our survey of [NiFe] structures from the Protein Data Bank[2−14] (Figure 3). A survey of catalytic rates of different bacterium species and their corresponding active site structures showed that certain cysteinate arrangements around the nickel ion favorably influence hydrogenase activity (Table 2). Correspondingly, our parametrization and molecular dynamics results showed differences in the flexibility of the cysteinates bound to the active site metal ions in the Ni−B and Ni−C catalytic states.

Assessment of Force-Field Quality and Transferability. We have derived classical force-field parameters for [NiFe] that result in normal modes reflective of those from DFT and yield stable MD simulations of [NiFe] hydrogenases in the oxidized and reduced catalytic states with a limited set of dihedral angles. The frequency-matching process helps to partition the DFT vibrational properties into bonded and nonbonded contributions as in eq 1. Therefore, the force constants should be transferrable to other force fields so long as the same connectivity is used. However, researchers should consider testing the atom-centered charges when using these derived parameters in united-atom force fields, since the treatment of nonbonded interactions is different.

[NiFe] Cα RMSD and intercluster distances are consistent with the initial structure and show no instabilities or unusual deformations, although it is not possible to fully assess the equilibration of such a large protein without much more conformational sampling. In the protein MD simulations, the Fe/S cluster side chain orientations maintain the initial configuration from 1YRQ.pdb. Protein hydrogen bonds allow inserted model active sites to adapt their cysteine angles from force-field equilibrium angles to the angles in the initial 1YRQ protein structure so the force field is likely to be transferrable to other [NiFe] structures. Furthermore, the average Ni−B and Ni−C active site geometries are comparable to oxidized and reduced structures from 1WUJ.pdb and 1WUL.pdb, respectively.

Potential Research Questions. The derived force field holds the potential for future simulations and improved mechanistic understanding of metal cluster function in these enzymes using higher-level methods such as QM/MM[64] and classical free energy perturbation (FEP).[65] MD and FEP calculations can calculate the effects of specific protein residue mutations on the structural, dynamic, and thermodynamic properties associated with catalytic activity. QM/MM molecular orbital calculations of metal clusters in different geometrical configurations in conjunction with experimental electron transfer rates[66] can be used to assess reorganization energies and the relative orientations of donor and acceptor orbitals in a context that explicitly includes the first and second coordination sphere backbone and side chain atoms.[60,62]

■ ASSOCIATED CONTENT

Ⓢ Supporting Information

Charges and bond, angle, and dihedral parameters for each of the metal centers listed in Table 1 (force constants from PE scans and frequency matching are included); *xyz* coordinates of the DFT-optimized Ni−B active site and reduced, distal Fe/S cluster models. This material is available free of charge via the Internet at http://pubs.acs.org.

■ AUTHOR INFORMATION

Corresponding Author
*E-mail: dayle.smith@pnl.gov.

Notes
The authors declare no competing financial interest.

■ ACKNOWLEDGMENTS

resources. PNNL is operated by the Battelle Memorial Institute for the United States Department of Energy.

■ REFERENCES

(1) Cammack, R. Bioinorganic chemistry - Hydrogenase sophistication. *Nature* **1999**, *397*, 214−215.

(2) Ogata, H.; Hirota, S.; Nakahara, A.; Komori, H.; Shibata, N.; Kato, T.; Kano, K.; Higuchi, Y. Activation process of NiFe hydrogenase elucidated by high-resolution X-ray analyses: Conversion of the ready to the unready state. *Structure* **2005**, *13*, 1635−1642.

(3) Garcin, E.; Vernede, X.; Hatchikian, E. C.; Volbeda, A.; Frey, M.; Fontecilla-Camps, J. C. The crystal structure of a reduced NiFeSe hydrogenase provides an image of the activated catalytic center. *Protein Struct. Anal., Folding Des.* **1999**, *7*, 557−566.

(4) Ogata, H.; Kellers, P.; Lubitz, W. The Crystal Structure of the NiFe Hydrogenase from the Photosynthetic Bacterium Allochromatium vinosum: Characterization of the Oxidized Enzyme (Ni-A State). *J. Mol. Biol.* **2010**, *402*, 428−444.

(5) Volbeda, A.; Charon, M. H.; Piras, C.; Hatchikian, E. C.; Frey, M.; Fontecilla-Camps, J. C. Crystal structure of the nickel-iron hydrogenase from desulfovibrio-gigas. *Nature* **1995**, *373*, 580−587.

(6) Leroux, F.; Dementin, S.; Burlatt, B.; Cournac, L.; Volbeda, A.; Champ, S.; Martin, L.; Guigliarelli, B.; Bertrand, P.; Fontecilla-Camps, J.; Rousset, M.; Leger, C. Experimental approaches to kinetics of gas diffusion in hydrogenase. *Proc. Natl. Acad. Sci. U. S. A.* **2008**, *105*, 11188−11193.

(7) Dementin, S.; Leroux, F.; Cournac, L.; de Lacey, A. L.; Volbeda, A.; Leger, C.; Burlat, B.; Martinez, N.; Champ, S.; Martin, L.; Sanganas, O.; Haumann, M.; Fernandez, V. M.; Guigliarelli, B.; Fontecilla-Camps, J. C.; Rousset, M. Introduction of Methionines in the Gas Channel Makes NiFe Hydrogenase Aero-Tolerant. *J. Am. Chem. Soc.* **2009**, *131*, 10156−10164.

(8) Matias, P. M.; Soares, C. M.; Saraiva, L. M.; Coelho, R.; Morais, J.; Le Gall, J.; Carrondo, M. A. NiFe hydrogenase from Desulfovibrio desulfuricans ATCC 27774: gene sequencing, three-dimensional structure determination and refinement at 1.8 angstrom and modelling studies of its interaction with the tetrahaem cytochrome c(3). *J. Biol. Inorg. Chem.* **2001**, *6*, 63−81.

(9) Higuchi, Y.; Ogata, H.; Miki, K.; Yasuoka, N.; Yagi, T. Removal of the bridging ligand atom at the Ni-Fe active site of NiFe hydrogenase upon reduction with H-2, as revealed by X-ray structure analysis at 1.4 angstrom resolution. *Protein Struct. Anal., Folding Des.* **1999**, *7*, 549−556.

(10) Volbeda, A.; Martin, L.; Cavazza, C.; Matho, M.; Faber, B. W.; Roseboom, W.; Albracht, S. P. J.; Garcin, E.; Rousset, M.; Fontecilla-Camps, J. C. Structural differences between the ready and unready oxidized states of NiFe hydrogenases (vol 10, pg 239, 2005). *J. Biol. Inorg. Chem.* **2005**, *10*, 591−591.

(11) Ogata, H.; Mizoguchi, Y.; Mizuno, N.; Miki, K.; Adachi, S.; Yasuoka, N.; Yagi, T.; Yamauchi, O.; Hirota, S.; Higuchi, Y. Structural studies of the carbon monoxide complex of NiFe hydrogenase from Desulfovibrio vulgaris Miyazaki F: Suggestion for the initial activation site for dihydrogen. *J. Am. Chem. Soc.* **2002**, *124*, 11628−11635.

(12) Volbeda, A.; Garcin, E.; Piras, C.; deLacey, A. L.; Fernandez, V. M.; Hatchikian, E. C.; Frey, M.; Fontecilla-Camps, J. C. Structure of the NiFe hydrogenase active site: Evidence for biologically uncommon Fe ligands. *J. Am. Chem. Soc.* **1996**, *118*, 12989−12996.

(13) Marques, M. C.; Coelho, R.; De Lacey, A. L.; Pereira, I. A. C.; Matias, P. M. The Three-Dimensional Structure of NiFeSe Hydrogenase from Desulfovibrio vulgaris Hildenborough: A Hydrogenase without a Bridging Ligand in the Active Site in Its Oxidised, "as-Isolated" State. *J. Mol. Biol.* **2010**, *396*, 893−907.

(14) Higuchi, Y.; Yagi, T.; Yasuoka, N. Unusual ligand structure in Ni-Fe active center and an additional Mg site in hydrogenase revealed by high resolution X-ray structure analysis. *Structure* **1997**, *5*, 1671−1680.

(15) Pandelia, M. E.; Ogata, H.; Lubitz, W. Intermediates in the Catalytic Cycle of NiFe Hydrogenase: Functional Spectroscopy of the Active Site. *ChemPhysChem* **2010**, *11*, 1127−1140.

(16) Dementin, S.; Burlat, B.; Fourmond, V.; Leroux, F.; Liebgott, P.-P.; Abou Hamdan, A.; Leger, C.; Rousset, M.; Guigliarelli, B.; Bertrand, P. Rates of Intra- and Intermolecular Electron Transfers in Hydrogenase Deduced from Steady-State Activity Measurements. *J. Am. Chem. Soc.* **2011**, *133*, 10211−10221.

(17) Tye, J. W.; Darensbourg, M. Y.; Hall, M. B. Refining the active site structure of iron-iron hydrogenase using computational infrared spectroscopy. *Inorg. Chem.* **2008**, *47*, 2380−8.

(18) Lubitz, W.; Reijerse, E.; van Gastel, M. [NiFe] and [FeFe] hydrogenases studied by advanced magnetic resonance techniques. *Chem. Rev.* **2007**, *107*, 4331−65.

(19) Helm, M. L.; Stewart, M. P.; Bullock, R. M.; DuBois, M. R.; DuBois, D. L. A Synthetic Nickel Electrocatalyst with a Turnover Frequency Above 100,000 s(-1) for H-2 Production. *Science* **2011**, *333*, 863−866.

(20) DuBois, M. R.; DuBois, D. L. The roles of the first and second coordination spheres in the design of molecular catalysts for H(2) production and oxidation. *Chem. Soc. Rev.* **2009**, *38*, 62−72.

(21) Nimlos, M. R.; Chang, C. H.; Curtis, C. J.; Miedaner, A.; Pilath, H. M.; DuBois, D. L. Calculated hydride donor abilities of five-coordinate transition metal hydrides HM(diphosphine)(2) (+) (M = Ni, Pd, Pt) as a function of the bite angle and twist angle of diphosphine ligands. *Organometallics* **2008**, *27*, 2715−2722.

(22) O'Hagan, M.; Shaw, W. J.; Raugei, S.; Chen, S.; Yang, J. Y.; Kilgore, U. J.; DuBois, D. L.; Bullock, R. M. Moving Protons with Pendant Amines: Proton Mobility in a Nickel Catalyst for Oxidation of Hydrogen. *J. Am. Chem. Soc.* **2011**, *133*, 14301−14312.

(23) Galvan, I. F.; Volbeda, A.; Fontecilla-Camps, J. C.; Field, M. J. A QM/MM study of proton transport pathways in a NiFe hydrogenase. *Proteins: Struct., Funct., Bioinf.* **2008**, *73*, 195−203.

(24) Montet, Y.; Amara, P.; Volbeda, A.; Vernede, X.; Hatchikian, E. C.; Field, M. J.; Frey, M.; Fontecilla-Camps, J. C. Gas access to the active site of Ni-Fe hydrogenases probed by X-ray crystallography and molecular dynamics. *Nat. Struct. Biol.* **1997**, *4*, 523−526.

(25) Teixeira, V. H.; Baptista, A. M.; Soares, C. M. Pathways of H-2 toward the active site of NiFe -hydrogenase. *Biophys. J.* **2006**, *91*, 2035−2045.

(26) Duan, Y.; Wu, C.; Chowdhury, S.; Lee, M. C.; Xiong, G. M.; Zhang, W.; Yang, R.; Cieplak, P.; Luo, R.; Lee, T.; Caldwell, J.; Wang, J. M.; Kollman, P. A point-charge force field for molecular mechanics simulations of proteins based on condensed-phase quantum mechanical calculations. *J. Comput. Chem.* **2003**, *24*, 1999−2012.

(27) Bruschi, M.; Zampella, G.; Fantucci, P.; De Gioia, L. DFT investigations of models related to the active site of NiFe and Fe hydrogenases. *Coord. Chem. Rev.* **2005**, *249*, 1620−1640.

(28) Wang, P. H.; Best, R. B.; Blumberger, J. Multiscale Simulation Reveals Multiple Pathways for H(2) and O(2) Transport in a NiFe -Hydrogenase. *J. Am. Chem. Soc.* **2011**, *133*, 3548−3556.

(29) van Gastel, M.; Fichtner, C.; Neese, F.; Lubitz, W. EPR experiments to elucidate the structure of the ready and unready states of the NiFe hydrogenase of Desulfolvibrio vulgaris Miyazaki F. *Biochem. Soc. Trans.* **2005**, *33*, 7−11.

(30) Stein, M.; Lubitz, W. DFT calculations of the electronic structure of the paramagnetic states Ni-A, Ni-B and Ni-C of NiFe hydrogenase. *Phys. Chem. Chem. Phys.* **2001**, *3*, 2668−2675.

(31) Volbeda, A.; Martin, L.; Cavazza, C.; Matho, M.; Faber, B. W.; Roseboom, W.; Albracht, S. P. J.; Garcin, E.; Rousset, M.; Fontecilla-Camps, J. C. Structural differences between the ready and unready oxidized states of NiFe hydrogenases. *J. Biol. Inorg. Chem.* **2005**, *10*, 239−249.

(32) Emptage, M. H.; Kent, T. A.; Huynh, B. H.; Rawlings, J.; Ormejohnson, W. H.; Munck, E. Nature of the iron-sulfur centers in a ferredoxin from *Azobacter vinlandii* - Mössbauer studies and cluster displacement experiments. *J. Biol. Chem.* **1980**, *255*, 1793−1796.

(33) Papaefthymiou, V.; Girerd, J. J.; Moura, I.; Moura, J. J. G.; Munck, E. Mössbauer study of *D-gigas* ferredoxin-II and spin-coupling model for the Fe3S4 cluster with valence delocalization. *J. Am. Chem. Soc.* **1987**, *109*, 4703−4710.

(34) Sondergaard, C. R.; Olsson, M. H. M.; Rostkowski, M.; Jensen, J. H. Improved Treatment of Ligands and Coupling Effects in Empirical Calculation and Rationalization of pK(a) Values. *J. Chem. Theory Comput.* **2011**, *7*, 2284−2295.

(35) Bylaska, E. J.; de Jong, W. A.; Govind, N.; Kowalski, K.; Straatsma, T. P.; Valiev, M.; Wang, D.; Apra, E.; Windus, T. L.; NWChem, A. *Computational Chemistry Package for Parallel Computers*, version 5.1.1; Pacific Northwest National Laboratory: Richland, WA, 2008.

(36) Chang, C. H.; Kim, K. Density Functional Theory Calculation of Bonding and Charge Parameters for Molecular Dynamics Studies on FeFe Hydrogenases. *J. Chem. Theory Comput.* **2009**, *5*, 1137−1145.

(37) Frisch, M. J.; Pople, J. A.; Binkley, J. S. Self-consistent molecular-orbital methods. 25. Supplementary functions for Gaussian basis sets. *J. Chem. Phys.* **1984**, *80*, 3265−3269.

(38) Wachters, A. J. Gaussian basis set for molecular wavefunctions containint third-row atoms. *J. Chem. Phys.* **1970**, *52*, 1033−1036.

(39) Schafer, A.; Horn, H.; Ahlrichs, R. Fully optimized contracted Gaussian basis sets for atoms Li to Kr. *J. Chem. Phys.* **1992**, *97*, 2571−2577.

(40) Humphrey, W.; Dalke, A.; Schulten, K. VMD: Visual molecular dynamics. *J. Mol. Graphics* **1996**, *14*, 33−38.

(41) Bayly, C. I.; Cieplak, P.; Cornell, W. D.; Kollman, P. A. A well-behaved electrostatic potential based method using charge restraints for deriving atomic charges - the RESP model. *J. Phys. Chem.* **1993**, *97*, 10269−10280.

(42) Fernandez-Alberti, S.; Bacelo, D. E.; Binning, R. C.; Echave, J.; Chergui, M.; Lopez-Garriga, J. Sulfide-binding hemoglobins: Effects of mutations on active-site flexibility. *Biophys. J.* **2006**, *91*, 1698−1709.

(43) de Hatten, X.; Cournia, Z.; Huc, I.; Smith, J. C.; Metzler-Nolte, N. Force-field development and molecular dynamics simulations of ferrocene-peptide conjugates as a scaffold for hydrogenase mimics. *Chemistry* **2007**, *13*, 8139−8152.

(44) Vaiana, A. C.; Cournia, Z.; Costescu, I. B.; Smith, J. C. AFMM: A molecular mechanics force field vibrational parametrization program. *Comput. Phys. Commun.* **2005**, *167*, 34−42.

(45) Brooks, B. R.; Bruccoleri, R. E.; Olafson, B. D.; States, D. J.; Swaminathan, S.; Karplus, M. CHARMM - A program for macro-molecular energy, minimization, and dynamics calculations. *J. Comput. Chem.* **1983**, *4*, 187−217.

(46) Lindahl, E.; Hess, B.; van der Spoel, D. GROMACS 3.0: a package for molecular simulation and trajectory analysis. *J. Mol. Model.* **2001**, *7*, 306−317.

(47) Hess, B. P-LINCS: A parallel linear constraint solver for molecular simulation. *J. Chem. Theory Comput.* **2008**, *4*, 116−122.

(48) Cheng, A. L.; Merz, K. M. Application of the Nose-Hoover chain algorithm to the study of protein dynamics. *J. Phys. Chem.* **1996**, *100*, 1927−1937.

(49) Parrinello, M.; Rahman, A. Polymorphic transitions in single crystals - a new molecular dynamics method. *J. Appl. Phys.* **1981**, *52*, 7182−7190.

(50) Mahoney, M. W.; Jorgensen, W. L. A five-site model for liquid water and the reproduction of the density anomaly by rigid, nonpolarizable potential functions. *J. Chem. Phys.* **2000**, *112*, 8910−8922.

(51) Dementin, S. b.; Leroux, F.; Cournac, L.; Lacey, A. L. d.; Volbeda, A.; Léger, C.; Burlat, B. n. d.; Martinez, N.; Champ, S. p.; Martin, L.; Sanganas, O.; Haumann, M.; Fernández, V. c. M.; Guigliarelli, B.; Fontecilla-Camps, J. C.; Rousset, M. Introduction of Methionines in the Gas Channel Makes [NiFe] Hydrogenase Aero-Tolerant. *J. Am. Chem. Soc.* **2009**, *131*, 10156−10164.

(52) Higuchi, Y.; Ogata, H.; Miki, K.; Yasuoka, N.; Yagi, T. Removal of the bridging ligand atom at the Ni Fe active site of [NiFe] hydrogenase upon reduction with H2, as revealed by X-ray structure analysis at 1.4 Å resolution. *Structure (London, U. K.)* **1999**, *7*, 549−556.

(53) Higuchi, Y.; Yasuoka, N.; Kakudo, M.; Katsube, Y.; Yagi, T.; Inokuchi, H. Single crystals of hydrogenase from Desulfovibrio vulgaris Miyazaki F. *J. Biol. Chem.* **1987**, *262*, 2823−2825.

(54) Leroux, F.; Dementin, S.; Burlat, B.; Cournac, L.; Volbeda, A.; Champ, S.; Martin, L.; Guigliarelli, B.; Bertrand, P.; Fontecilla-Camps, J.; Rousset, M.; Léger, C. Experimental approaches to kinetics of gas diffusion in hydrogenase. *Proc. Natl. Acad. Sci.* **2008**, *105*, 11188−11193.

(55) Ogata, H.; Kellers, P.; Lubitz, W. The Crystal Structure of the [NiFe] Hydrogenase from the Photosynthetic Bacterium Allochromatium vinosum: Characterization of the Oxidized Enzyme (Ni-A State). *J. Mol. Biol.* **2010**, *402*, 428−444.

(56) Shomura, Y.; Yoon, K.-S.; Nishihara, H.; Higuchi, Y. Structural basis for a [lsqb]4Fe-3S[rsqb] cluster in the oxygen-tolerant membrane-bound [lsqb]NiFe[rsqb]-hydrogenase. *Nature* **2011**, *479*, 253−256.

(57) Volbeda, A.; Martin, L.; Cavazza, C.; Matho, M.; Faber, B. W.; Roseboom, W.; Albracht, S. P. J.; Garcin, E.; Rousset, M.; Fontecilla-Camps, J. C. Structural differences between the ready and unready oxidized states of [NiFe] hydrogenases. *J. Biol. Inorg. Chem.* **2005**, *10*, 239−249.

(58) Szilagyi, R. K.; Winslow, M. A. On the accuracy of density functional theory for iron - Sulfur clusters. *J. Comput. Chem.* **2006**, *27*, 1385−1397.

(59) Jensen, K. P. Computational studies of modified Fe3S4 clusters: Why iron is optimal. *J. Inorg. Biochem.* **2008**, *102*, 87−100.

(60) Sigfridsson, E.; Olsson, M. H. M.; Ryde, U. Inner-sphere reorganization energy of iron-sulfur clusters studied with theoretical methods. *Inorg. Chem.* **2001**, *40*, 2509−2519.

(61) Li, J. B.; Zhu, T. H.; Cramer, C. J.; Truhlar, D. G. New class IV charge model for extracting accurate partial charges from wave functions. *J. Phys. Chem. A* **1998**, *102*, 1820−1831.

(62) Noodleman, L.; Lovell, T.; Liu, T. Q.; Himo, F.; Torres, R. A. Insights into properties and energetics of iron-sulfur proteins from simple clusters to nitrogenase. *Curr. Opin. Chem. Biol.* **2002**, *6*, 259−273.

(63) Mitra, D.; Pelmenschikov, V.; Guo, Y. S.; Case, D. A.; Wang, H. X.; Dong, W. B.; Tan, M. L.; Ichiye, T.; Jenney, F. E.; Adams, M. W. W.; Yoda, Y.; Zhao, J. Y.; Cramer, S. P. Dynamics of the 4Fe-4S Cluster in Pyrococcus furiosus D14C Ferredoxin via Nuclear Resonance Vibrational and Resonance Raman Spectroscopies, Force Field Simulations, and Density Functional Theory Calculations. *Biochemistry* **2011**, *50*, 5220−5235.

(64) Siegbahn, P. E. M.; Himo, F. Recent developments of the quantum chemical cluster approach for modeling enzyme reactions. *J. Biol. Inorg. Chem.* **2009**, *14*, 643−651.

(65) Long, H. K. P. W. G. M. L. K. K. Hydrogenase/ferredoxin charge-transfer complexes: effect of hydrogenase mutations on the complex association. *J. Phys. Chem. A* **2009**, *113*, 4060−4067.

(66) Dementin, S.; Burlat, B.; Fourmond, V.; Leroux, F.; Liebgott, P. P.; Abou Hamdan, A.; Leger, C.; Rousset, M.; Guigliarelli, B.; Bertrand, P. Rates of Intra- and Intermolecular Electron Transfers in Hydrogenase Deduced from Steady-State Activity Measurements. *J. Am. Chem. Soc.* **2011**, *133*, 10211−10221.